# Molecular Dynamics Simulation of Laser Melting of Nanocrystalline Au[†]

**Zhibin Lin,[‡,§] Elodie Leveugle,[‡,||] Eduardo M. Bringa,[⊥] and Leonid V. Zhigilei*[,‡]**

*Department of Materials Science and Engineering, University of Virginia, 395 McCormick Road, Charlottesville, Virginia 22904-4745, Renewable Energy Materials Research Science and Engineering Center (REMRSEC), Department of Physics, Colorado School of Mines, Golden, Colorado 80401, Thales Research and Technology - France, 91767 Palaiseau Cedex, France, and Instituto de Ciencias Básicas, Universidad Nacional de Cuyo, M5502JMA Mendoza, Argentina*

*Received: September 28, 2009; Revised Manuscript Received: November 7, 2009*

The mechanisms and kinetics of short pulse laser melting of single crystal and nanocrystalline Au films are investigated on the basis of the results of simulations performed with a model combining the molecular dynamics method with a continuum-level description of the laser excitation and subsequent relaxation of the conduction band electrons. A description of the thermophysical properties of Au that accounts for the contribution of the thermal excitation of d band electrons is incorporated into the model and is found to play a major role in defining the kinetics of the melting process. The effect of nanocrystalline structure on the melting process is investigated for a broad range of laser fluences. At high fluences, the grain boundary melting in nanocrystalline films results in a moderate decrease of the size of the crystalline grains at the initial stage of the laser heating and is followed by a rapid (within several picoseconds) collapse of the crystal structure in the remaining crystalline parts of the film as soon as the lattice temperature exceeds the limit of the crystal stability against the onset of rapid homogeneous melting (the limit of superheating). At low laser fluences, close to the threshold for the complete melting of the film, the initiation of melting at grain boundaries can steer the melting process along the path where the melting continues below the equilibrium melting temperature and the crystalline regions shrink and disappear under conditions of substantial undercooling. The unusual melting behavior of nanocrystalline films is explained on the basis of thermodynamic analysis of the stability of small crystalline clusters surrounded by undercooled liquid.

## 1. Introduction

It is well established that free surfaces and crystal defects play a prominent role in the initiation of melting.[1−6] Under conditions of slow heating, the melting process starts from surfaces and internal crystal defects under rather minor superheating conditions or even below the equilibrium melting temperature. The later effect of surface premelting is observed when the free surface wetted by a thin liquid layer has a lower free energy as compared to the ordered solid surface.[3] After heterogeneous nucleation of the liquid phase, the melting process proceeds by propagation of melting fronts from the surfaces and defect regions, precluding any significant superheating of the remaining crystalline parts of the material and eliminating the possibility for an alternative mode of melting, homogeneous nucleation of liquid in the bulk of a superheated crystal.

It has been reported that a substantial superheating above the equilibrium melting point can be achieved in defect-free thin films or small particles when the surface melting is suppressed, e.g., by coating the surface with a high melting point material that eliminates the free surface and creates a low-energy epitaxial interface instead.[6−10] The melting process in these systems is largely controlled by the nature of the interfaces, making it difficult to directly relate the observed superheating to the theoretical predictions on the stability of the crystalline phase and the limit of superheating.[11−15]

An alternative method to suppress the heterogeneous melting is to create the heating conditions that would kinetically limit the contribution of the melting front propagation to the melting process.[16] Irradiation by short (pico- and femtosecond) laser pulses, in particular, can result in extremely high heating rates exceeding $10^{14}$ K/s, making the time of the temperature increase shorter than the time needed for any significant advancement of the melting front. Indeed, investigations of the short pulse laser melting with optical, X-ray, and electron diffraction time-resolved probe techniques have provided valuable information on the characteristic time-scales and mechanisms of melting occurring under conditions of strong superheating.[17−26]

The interpretation of the results of the experimental probing of the fast laser-induced phase transformations has been assisted by molecular dynamics (MD) simulations that are well suited for investigation of ultrafast processes and are capable of providing detailed atomic-level information on the structural changes in the irradiated targets. MD modeling of laser melting and resolidification of bulk metal targets[27−33] and thin films of various thickness[34−39] has revealed a wealth of information on the microscopic mechanisms and kinetics of the melting process occurring under conditions of the fast laser energy deposition. In particular, the relative contributions of the homogeneous and heterogeneous melting mechanisms have been analyzed and related to the irradiation conditions in simulations performed for Ni, Au, Al, and Cu thin films,[34−39] bulk targets,[33] and metal bilayer systems[32] irradiated by short, from 200 fs to 150 ps, laser pulses. The lattice distortions associated with relaxation

[†] Part of the "Barbara J. Garrison Festschrift".

* Author to whom correspondence should be addressed. E-mail: lz2n@virginia.edu.

[‡] University of Virginia.

[§] Colorado School of Mines.

[||] Thales Group.

[⊥] Universidad Nacional de Cuyo.

10.1021/jp909328q 
Published on Web 12/02/2009

of laser-induced stresses have been found to significantly reduce the crystal stability against melting, resulting in homogeneous nucleation of the liquid phase at temperatures close to the equilibrium melting temperature.[35] The calculations of the diffraction profiles and density correlation functions have been used to establish direct connections between the results of MD simulations and time-resolved diffraction experiments.[38,39]

Despite the active experimental and computational investigations of the mechanisms of laser melting, the question on the effect of the microstructure (the arrangement of crystal defects in a crystalline material) of the irradiated target on the melting process remains largely unexplored. In all MD simulations of laser melting performed so far, computational systems have been represented by single crystals with no internal defects present in the initial state. The experimental targets, on the other hand, are often polycrystalline and, in addition to grain boundaries, may have other crystal defects introduced in the process of sample preparation. For example, the free-standing 20-nm-thick films prepared by thermal deposition and used in time-resolved electron diffraction experiments[20,22,26] are likely to have nanocrystalline structure with the average grain size comparable to the thickness of the film. The results of MD simulations of heat treatment and melting of nanocrystalline materials, performed under conditions of constant temperature and pressure, demonstrate a profound effect of nanostructure on the thermal stability of the material. For example, an investigation of the grain growth kinetics in nanocrystalline Ni at temperatures ranging from about 10 to 45% below the melting temperature reveals a linear increase of the average grain size with time due to the size-dependent mobility of the grain boundaries.[40] A continuous melting process starting from grain boundaries and proceeding at temperatures below the melting temperature of a single crystal is observed in MD simulations of nanocrystalline Ag.[41,42] A substantial decrease of the melting temperature with decreasing mean grain size is predicted in these simulations and related to the size-dependent melting temperature of the corresponding nanoparticles. Under conditions of fast laser heating, however, the contribution of the grain-boundary-nucleated melting[5] can be kinetically limited by the relatively low maximum velocity of the melting front propagation,[16] making the applicability of the results obtained under constant temperature conditions questionable. The characteristics of the laser melting process are likely to be defined by both the size/microstructure-dependent thermodynamic driving forces and the kinetics of heterogeneous and homogeneous melting processes.

To investigate the effect of grain boundaries and nanocrystalline microstructure on the characteristics of the laser melting process, we perform MD simulations of short pulse laser melting of thin Au films with nanocrystalline and single crystal structures. The effect of the nanocrystalline structure on the melting process is investigated for different irradiation conditions, with theoretical analysis based on the classical nucleation theory used for interpretation of the computational results. The method used for generation of the initial nanocrystalline system and the computational model used in the MD simulations of laser melting of metal films are briefly described next, in section 2. The results of the simulations are presented and discussed in section 3 and summarized in section 4.

## 2. Computational Model

The MD simulations of short pulse laser melting are performed for 20 nm Au films with single crystal and nanocrystalline structures. In the case of single crystal films, the initial system is a face centered cubic (fcc) crystal composed of 500 000 atoms with dimensions of $20.46 \times 20.46 \times 20.46$ nm$^3$ and periodic boundary conditions imposed in the directions parallel to two (001) free surfaces. The single crystal films are similar to the ones used in earlier simulations of laser melting.[38] These earlier simulations were done without accounting for the effect of the thermal excitation of electrons from states located below the Fermi level on the electron temperature dependences of the electron−phonon coupling and electron heat capacity.[43,44] It was recently shown, however, that the kinetics of the melting process can be strongly affected by the transient modification of the thermophysical properties of Au related to the thermal excitation of d band electrons under conditions of strong laser-induced electron−phonon nonequilibrium.[44] The time of the beginning of melting, in particular, can be overpredicted by as much as a factor of 2 if the contribution of the d band electrons is not accounted for in the temperature dependences of the thermophysical properties. Therefore, the simulations of laser melting of single crystal films are repeated in this study with a more accurate parametrization of the model. The effect of the thermal excitation of the d band electrons on the results of the simulations is discussed in section 3.1.

The initial structure of the nanocrystalline Au film is constructed using the Voronoi tessellation method.[45−48] Briefly, the atomic structure of the film is generated as follows. First, the positions of centers of 31 grains to be created are distributed randomly within the MD computational system of the same dimensions as the ones used for the single crystal film discussed above. Randomly oriented fcc crystallites are then built around each center so that any atom that belongs to a given grain is closer to the center of this grain than to any of the centers of other grains. If two atoms that belong to different grains are found to be closer than 80% of the fcc nearest-neighbor distance to each other, one of the atoms is removed to avoid generation of local atomic configurations with unrealistically high energies. To allow for the structural relaxation of the nanocrystalline system, the atomic configuration is equilibrated in a MD simulation performed at 300 K for a period of 450 ps.

The atomic structure of equilibrated nanocrystalline film is shown in Figure 1. The atoms are colored according to the centrosymmetry parameter[49] calculated for each atom using the following definition:

$$\Phi = \sum_{i=1}^{6} |\vec{R}_i + \vec{R}_{-i}|^2 \quad (1)$$

where $\vec{R}_i$ and $\vec{R}_{-i}$ are pairs of vectors that connect the atom of interest to the opposite nearest neighbors in the fcc lattice. The value of the centrosymmetry parameter is zero for atoms with a perfect fcc surroundings and sharply increases as the local atomic environment deviates from the fcc centrosymmetry. In addition to the identification of the grain boundaries in the nanocrystalline film, we use the centrosymmetry parameter to distinguish between the crystalline and liquid regions of the film in the simulations of laser melting. In order to reduce the thermal noise in atomic positions, the generation of snapshots of atomic configurations and calculation of the centrosymmetry parameter are preceded by quenching each atomic configuration for 5 ps using a velocity dampening technique, where the velocity of each individual atom is set to zero at the time when the kinetic energy of the atom maximizes. The fast quenching does not introduce any structural changes to the atomic configurations but makes the visualization and structural analysis more straightforward.

The total number of Au atoms in the nanocrystalline system is 486 861, and the density is 98.6% of the density of the single

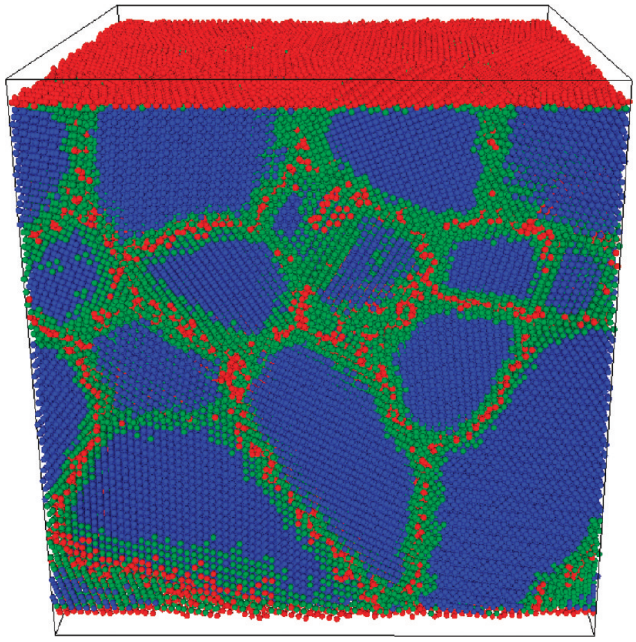

**Figure 1.** Atomic configuration of nanocrystalline film used in the simulation of laser melting. Atoms are colored according to the centrosymmetry parameter, from blue color corresponding to atoms with local fcc surroundings ($\Phi < 0.1$) to green and red colors corresponding to atoms at the free surfaces and in the grain boundary regions ($0.1 < \Phi < 8$ for green and $\Phi > 8$ for red).

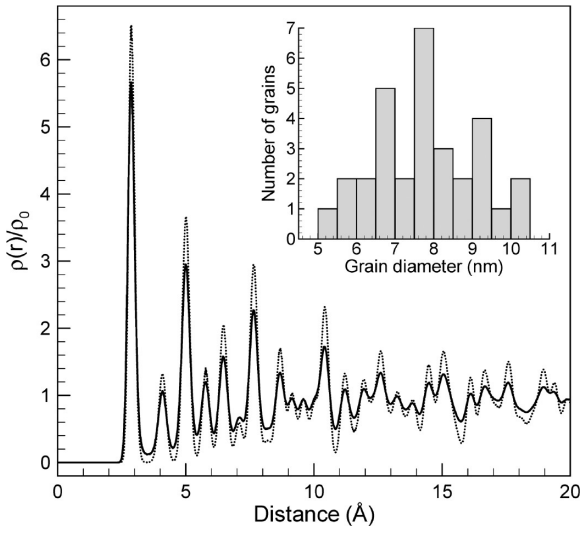


**Figure 2.** Pair density functions of nanocrystalline (solid line) and single crystal (dotted line) Au films equilibrated at 300 K. The functions are normalized by the average densities of the corresponding films. The inset shows the distribution of grain sizes in the nanocrystalline film. The diameters of the grains are calculated from the corresponding volumes of Voronoi polyhedra assuming spherical shapes of the grains.

crystal. The high density of the model nanocrystalline material is consistent with experimental measurements reported for nanocrystalline Au (mean grain size 20−60 nm) prepared by the vapor deposition method.[50] It is known that for a large number of grains the Voronoi tessellation produces a grain size distribution that is close to a log-normal distribution.[51] The nanocrystalline sample generated in this work consists of 31 grains, with the grain size distribution shown in the inset of Figure 2. The average grain diameter, calculated by assuming spherical shapes of the grains, is ∼8 nm. Similar to the single crystal films described above, periodic boundary conditions are imposed in the directions parallel to the two free surfaces of the nanocrystalline film. The periodic boundary conditions provide an adequate representation of the experimental conditions where the laser spot diameter is much larger than the size of the computational cell and the energy redistribution in the lateral directions can be neglected on the time-scales considered in the simulations.

The difference in the atomic structure of the single crystal and nanocrystalline films can be illustrated by pair density functions (PDFs) calculated for the two systems at 300 K and shown in Figure 2. The PDFs represent the correlations in atomic positions in the systems and are defined as[38,52]

$$\rho(r) = \frac{1}{2\pi N r^2} \sum_{j=1}^{N} \sum_{i<j}^{N} \delta(r - r_{ij}) \qquad (2)$$

where $r_{ij}$ is the distance between atoms $i$ and $j$, $N$ is the number of atoms in the system, and $\delta$ is the Dirac delta function. The lower intensities of the correlation peaks at characteristic interatomic distances corresponding to several closest fcc neighbor shells and higher intensities at distances between the peaks, observed for the nanocrystalline system, are related to the substantial fraction of atoms that belong to the grain boundary regions and do not have local fcc surroundings. The increase in the difference between the peak intensities at larger distances corresponds to the loss of the correlation in atomic positions upon passing from one grain to another. The widths of the PDF peaks are mainly defined by the thermal vibrations of the atoms (i.e., the Debye−Waller factor[53]) and are similar in the two PDFs calculated for the two different structures at the same temperature of 300 K.

The simulations of laser interaction with Au films are performed with a hybrid atomistic-continuum model that couples the classical MD method with a continuum-level description of the laser excitation and subsequent relaxation of the conduction band electrons. The model is based on the well-known two-temperature model[54] (TTM) that describes the time evolution of the lattice and electron temperatures in the irradiated target by two coupled nonlinear differential equations. In the combined TTM-MD model, MD substitutes the TTM equation for the lattice temperature. The TTM equation for the electron temperature is solved by a finite difference method simultaneously with MD integration of the equations of motion of atoms. The electron temperature enters a coupling term that is added to the MD equations of motion to account for the energy exchange between the electrons and the lattice. The cells in the finite-difference discretization are related to the corresponding volumes of the MD system, and the local lattice temperature is defined for each cell from the average kinetic energy of thermal motion of atoms. A complete description of the combined TTM-MD model is given in ref 34.

The interatomic interaction in the MD part of the model is described by the embedded atom method (EAM) with the functional form and parametrization suggested by Johnson and given in ref 55. The EAM potential defines all of the thermal and elastic properties of the material. Some of the physical properties of EAM Au relevant to the material response to the laser heating are given in ref 38. In particular, the values of the equilibrium melting temperature $T_m$ and enthalpy of melting $\Delta H_m$ predicted by the EAM Au potential at zero pressure are 963 K and 8.4 kJ mol$^{-1}$, compared to the corresponding experimental values[56] of 1336 K and 12.8 kJ mol$^{-1}$. The equilibrium melting temperature is determined from liquid-crystal coexistence simulations,[34,57] and the enthalpy of melting is found from the difference between the values of enthalpy of the liquid and crystalline phases equilibrated at $T_m$ and zero

pressure.[34] Despite the significant quantitative discrepancies between the properties of the model EAM Au and real Au, the knowledge of the thermodynamic properties of the model material allows us to perform a quantitative analysis and physical interpretation of the simulation results, as well as to map the results of the simulations to experimental data.

The electron temperature dependences of the thermophysical material properties included in the TTM equation for the electron temperature (the electron−phonon coupling factor, the electron heat capacity, and the thermal conductivity) are taken in the forms that account for the contribution from the thermal excitation from the electron states below the Fermi level.[43,44] As discussed in section 3.1, the large positive deviations of the electron heat capacity from the linear dependence and the sharp increase in the strength of the electron−phonon coupling, predicted for Au at electron temperatures exceeding 3000 K, have a significant effect on the kinetics of the laser melting process. Note that electron scattering at grain boundaries can be expected to increase the effective strength of the electron–phonon coupling in the nanocrystalline film as compared to the single crystal film.[58,59] Indeed, a substantial enhancement of the rate of the electron−phonon equilibration has been observed in pump−probe experiments performed for nanocrystalline films[60,61] and nanoparticles.[62] Using experimental data of ref 61 and following the theoretical analysis of refs 58 and 61, the electron scattering at grain boundaries can be estimated to almost double the effective strength of the electron−phonon coupling for the 20 nm film with an average grain size of 8 nm. Due to the large uncertainty involved in the quantitative evaluation of the electron-boundary scattering, however, we chose to neglect the contribution of the grain boundaries to the electron−phonon equilibration process. The assumption of the same strength of the electron−phonon coupling in the two systems allows us (1) to perform a direct comparison between the results obtained for single crystal and nanocrystalline films at the same rate of the lattice heating and (2) to separate the structural and thermodynamic aspects of the effect of grain boundaries on the kinetics of laser melting from the possible additional contribution due to the modification of the lattice heating rate.

Irradiation by a 200 fs laser pulse is represented through a source term with a Gaussian temporal profile and an exponential attenuation of laser intensity with depth under the surface (Beer−Lambert law) added to the TTM equation for the electron temperature.[34] The increase of the effective depth of the laser energy deposition due to the "ballistic" energy transfer by nonthermal electrons occurring before the thermalization of the excited electrons[63,64,65] is accounted for through modification of the optical absorption depth in the source term of the TTM equation.[34,38,63] Since the "ballistic range" in Au exceeds the thickness of the films considered in this work, 20 nm, the reflection of the nonthermal electrons from the back surface of the film results in a uniform distribution of the electron temperature established on the time scale of the electron thermalization.

## 3. Results and Discussion

In this section, the results of the simulations of laser melting of nanocrystalline Au films are presented and compared with the results obtained for single crystal films. The mechanisms and kinetics of laser melting of single crystal films are briefly discussed first, followed by the analysis of the distinctive features of the melting process in nanocrystalline films. An interpretation of the effect of the nanocrystalline structure of the film on the melting process, observed in the simulations, is provided on the basis of thermodynamic analysis of the stability of solid clusters surrounded by undercooled liquid.

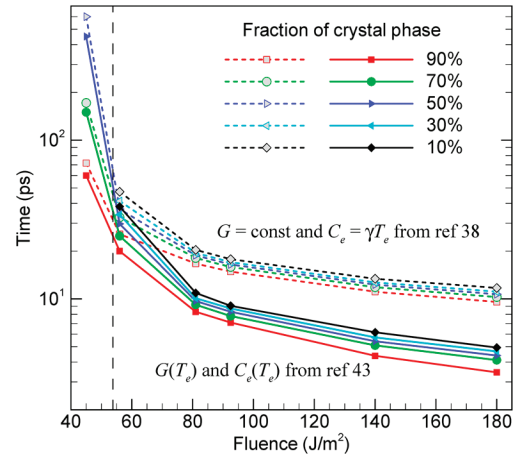


**Figure 3.** Time scales of the melting process in a 20 nm single crystal Au film irradiated with a 200 fs laser pulse at different absorbed fluences. Semilogarithmic plots of the time required to melt certain fractions of the film are shown. Each curve corresponds to a particular fraction of the remaining crystal phase as a function of the absorbed fluence. The atoms in the crystal phase are distinguished from the ones in the liquid phase on the basis of the local order parameter.[34,38,57] Solid lines show the results of simulations performed with the electron temperature ($T_e$) dependences of the electron heat capacity ($C_e$) and electron−phonon coupling ($G$) that account for the contribution of thermally excited d band electrons.[43] Dashed lines show the results from ref 38 calculated with the conventional temperature dependences of the thermophysical parameters. The vertical dashed line shows the value of the absorbed fluence that supplies the amount of energy necessary for the complete melting of the film.

**3.1. Laser Melting of Single Crystal Films: Effect of the Thermal Excitation of d Band Electrons.** The mechanisms and kinetics of short pulse laser melting of 20 nm single crystal Au films have been analyzed in detail in ref 38 based on the results of TTM-MD simulations performed with commonly used approximations of a constant electron−phonon coupling factor and a linear temperature dependence of the electron heat capacity. Here, we compare the predictions of these earlier simulations with the results obtained using a more realistic description of the electron temperature dependence of the thermophysical properties of Au that accounts for the contribution of the thermal excitation of electrons from states located below the Fermi level.[43]

The time scales of laser melting observed in the two series of TTM-MD simulations of single crystal Au films irradiated with 200 fs laser pulses can be compared in Figure 3, where the changes in the fraction of the crystal phase in the irradiated targets are shown. Two distinct melting regimes can be identified in both series of simulations. At fluences below ∼53 J/m$^2$, the melting proceeds by the propagation of two melting fronts from the free surfaces of the film and does not result in the complete melting of the film. At fluences above ∼70 J/m$^2$, the melting process is dominated by homogeneous nucleation of a large number of liquid regions inside the overheated crystal, resulting in the fast phase transformation in the entire film within just several picoseconds. In the intermediate regime, between 53 and 70 J/m$^2$, both the melting front propagation from the surfaces and homogeneous nucleation of liquid regions contribute to the melting process. The vertical dashed line in Figure 3 marks the absorbed fluence of 53.8 J/m$^2$ that supplies the amount of energy needed to heat the model material from 300 K to the equilibrium melting temperature and to melt the entire film at the melting temperature.[38]

The maximum fluence of 180 J/m$^2$ is chosen to avoid spallation/disintegration of the film.[34,37,66−70] The threshold fluence for disintegration of the film is predicted to be ∼250 J/m$^2$ in simulations performed with the new parametrization of the model (contribution of thermally excited d band electrons is included), and is significantly higher with the conventional temperature dependences of the parameters of the model. The difference in the spallation/disintegration thresholds can be explained by the faster rate of the electron−phonon energy transfer predicted with the new parametrization, leading to the generation of stronger compressive stresses during the time of the electron−phonon equilibration. The relaxation of the laser induced stresses in this case leads to the appearance, growth, and percolation of multiple voids[70] at temperatures significantly below the temperatures required for explosive boiling.[33,71] The contribution of the laser-induced stresses is negligible in simulations performed with the conventional set of parameters, where the disintegration of the film coincides with the onset of the explosive boiling of the overheated liquid.

A comparison between the melting times predicted in the two series of simulations (Figure 3) suggests that the starting time of the melting process shifts to earlier times and the duration of the melting process decreases when the effect of the thermal excitation of d band electrons on the thermophysical properties of the material is accounted for in the model. The difference in the starting times of the melting process is particularly large at high fluences. In particular, the time of the beginning of the melting process (defined as the time when the fraction of the melted material in the irradiated film reaches 10%) predicted with the new and old sets of parameters is 3.5 and 9.6 ps at 180 J/m$^2$, 4.4 and 11.1 ps at 140 J/m$^2$, 8.3 and 16.7 ps at 81 J/m$^2$, and 60 and 72 ps at 45 J/m$^2$, respectively. Thus, the difference in the predictions of the two models ranges from ∼20% at 45 J/m$^2$ to almost 3 times at 180 J/m$^2$. The large difference in the starting times of the melting process can be explained by the faster electron−phonon equilibration in the simulations where the increase in the strength of the electron–phonon coupling at high electron temperatures is taken into account.

The effect of the new parametrization of the model on the duration of the melting process is less pronounced, with the melting time (defined as the time needed for the melted fraction of the film to increase from 10 to 90%) changing from 2.6 ps at 81 J/m$^2$ to 1.5 ps at 180 J/m$^2$ with the new parameters and from 3.7 ps at 81 J/m$^2$ to 2.2 ps at 180 J/m$^2$ with the old parameters of the model. At a lower fluence of 56 J/m$^2$, close to the threshold for the complete melting of the film, the melting starts at 20 ps and takes 18 ps with the new parameters and starts at 26 ps and takes 22 ps with the old parameters of the model.

The predictions of the simulations can be related to the results of time-resolved electron diffraction measurements performed for a 20 nm Au film irradiated by a 200 fs laser pulse. The experimental results obtained for absorbed laser fluences of 119 J/m$^2$ (ref 22) and 137 J/m$^2$ (ref 23) indicate that the melting process starts at ∼7 ps and takes approximately 3 ps to melt the entire film. The melting temperature of the EAM Au material is lower than the experimental melting temperature of Au by about 28%, and somewhat lower absorbed laser fluences in the range 85−100 J/m$^2$ correspond to the overheating conditions realized in the experiment.[44] As can be seen from Figure 3, in this range of laser fluences, the time of the beginning of the melting process predicted with the new set of parameters is in excellent agreement with experimental data, whereas the simulations performed with the old set of parameters[38] (constant electron−phonon coupling factor and linear temperature dependence of the electron heat capacity) overpredict the starting time of the melting process by as much as a factor of 2. Therefore, the simulations discussed below are performed with the new set of parameters[43] that provide a realistic description of the lattice heating rate and the kinetics of the laser melting process.

**3.2. Laser Melting of Single Crystal Films: Microscopic Mechanisms.** Two laser fluences at the upper and lower ends of the range of fluences shown in Figure 3, 45 and 180 J/m$^2$, are chosen for investigation of the effect of the nanocrystalline structure on the melting process. For the single crystal films, the results of the simulations are illustrated in Figures 4−6. The evolution of average electron and lattice temperatures in the irradiated films is shown in Figure 4. Due to the small electron heat capacity, the laser energy deposition transiently brings the electron temperature up to very high values of 6190 and 10770 K at laser fluences of 45 and 180 J/m$^2$, respectively. The subsequent energy transfer to the lattice leads to a sharp drop in the electron temperature and an increase in the lattice temperature. As briefly discussed in section 2, the "ballistic" energy transfer by nonthermal electrons and relatively weak electron−phonon coupling in Au result in the establishment of a uniform distribution of the electron temperature throughout the 20 nm film during the time of the electron−phonon equilibration. As a result, the whole film is heated up uniformly and no significant variations of the electron and lattice temperatures are observed within the film at any time during the simulations (e.g., see ref 38, where the spatial and temporal distribution of the lattice temperature is shown for one of the simulations performed for a single crystal Au film). Therefore, the average electron and lattice temperatures shown in the temperature plots provide an adequate representation of the temperature evolution in the irradiated films.

At a fluence of 180 J/m$^2$, the lattice temperature exceeds the equilibrium melting temperature at 1.5 ps and continues to increase up to ∼50 ps. At later times, the temperature oscillates around the average value of 3310 K ($3.44T_m$), as can be seen from the inset in Figure 4a. The temperature oscillations are related to the corresponding elastic vibration of the film triggered by the buildup of the compressive stresses in the central part of the film during the first several picoseconds of the laser heating.[44] The relaxation of the compressive stresses drives the expansion of the film and initiates the vibration of the film that gradually dissipates with time but is still noticeable at the end of the simulation, at 400 ps. The oscillations of the lattice temperature are directly connected to the pressure oscillations in the film, with compression causing the temperature increase and expansion leading to cooling. Quantitative thermodynamic analysis performed in refs 34 and 35 confirms that the temperature variations with pressure can be attributed to the adiabatic/isentropic expansion/compression of the film. Note that, at lower laser fluences, below the threshold for laser melting, the excitation of the elastic vibration of the film (or coherent acoustic phonons) is reflected in periodic oscillations of the positions of diffraction peaks. This effect has been predicted in TTM-MD simulations[39] and observed in time-resolved electron and X-ray diffraction experiments.[72−74]

The atomic-level view of the melting process, shown for the fluence of 180 J/m$^2$ in Figure 5, can be related to the evolution of the lattice temperature discussed above. By the time of 2 ps, the lattice temperature exceeds the level of $\sim 1.25T_m$ that corresponds to the limit of crystal stability against the onset of

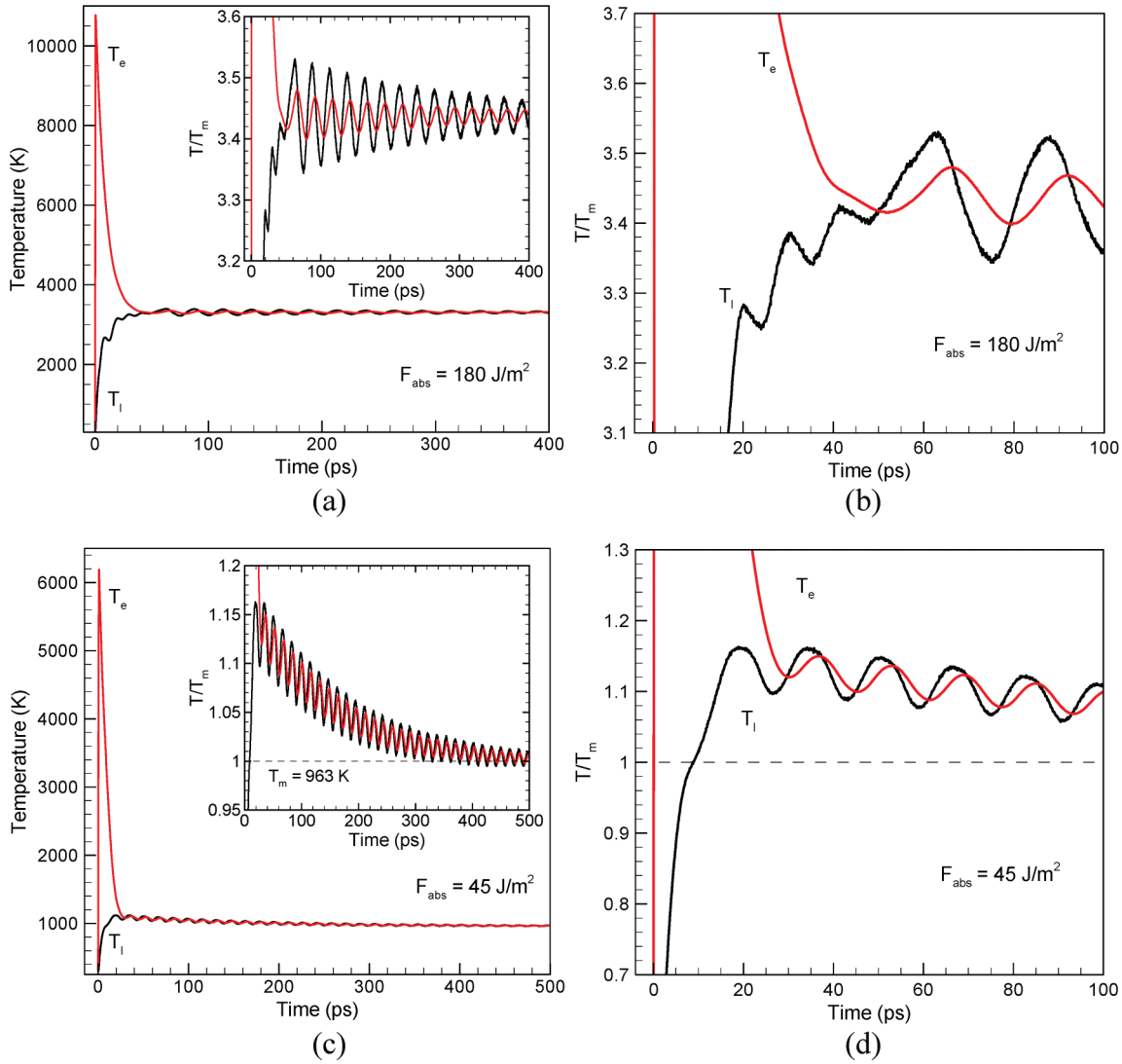


**Figure 4.** Temporal evolution of the average electron and lattice temperatures, $T_e$ and $T_l$, obtained in TTM-MD simulations of single crystal Au films irradiated by 200 fs laser pulses at absorbed fluences of 180 J/m$^2$ (a,b) and 45 J/m$^2$ (c,d). The horizontal dashed lines in panels c and d mark the equilibrium melting temperature of the EAM Au, $T_m$. In panels b and d and in the insets in panels a and c, the temperature is normalized by the equilibrium melting temperature, and the scale is chosen to show a closer view of the evolution of the electron and lattice temperatures during and after the melting process.

massive homogeneous melting.[34,35,38,75,76] The overheating above the limit of crystal stability results in the collapse of the crystal structure within the next 3 ps. Rapid nucleation and growth of liquid regions throughout the film is preceded by generation of a large number of point defects (vacancy−interstitial pairs) that can be identified in the snapshots shown for the time of 4 ps in Figure 5b and e. With the visualization method used in Figure 5, the point defects show up as clusters of atoms with elevated values of the centrosymmetry parameter. The interstitials introduce larger lattice distortions and appear in Figure 5e as large green clusters, whereas vacancies are represented by the smaller red clusters of 12 nearest neighbors of the missing atoms. The melting is largely completed by 5 ps, with only a few small remaining crystalline regions visible in Figure 5f.

The mechanism of the ultrafast homogeneous melting occurring under conditions of strong overheating is different from the classical picture of a homogeneous phase transformation that considers the nucleation and growth of well-defined spherical regions of a new phase.[15,77] There is no time for the system to minimize the liquid-crystal interfacial energy, and the melting proceeds as a rapid collapse of the lattice overheated above the limit of its stability. The time required for melting of the strongly overheated crystal is comparable to several periods of atomic vibrations and can be considered as the minimum time required for the thermal melting of an overheated material.[34,38] Indeed, the time scale of laser-induced melting measured for thin Al and Au films in time-resolved electron diffraction experiments[20,22,23] is in good agreement with the results of the simulations.[38,44]

Despite the large number of point defects observed in Figure 5e, the ultrafast melting observed in the simulation does not follow the scenario suggested in ref 78, where the formation of clusters of interstitials and vacancies is suggested as an intermediate step for the homogeneous nucleation of the liquid phase. The time scale of the melting process is too short to allow for the diffusional rearrangement of the point defects into clusters. Nevertheless, the lattice distortions associated with the large density of vacancies and interstitials are likely to create an overall "background" of the elevated potential energy in the crystal and contribute to the onset of the lattice instabilities and rapid collapse of the crystalline structure.

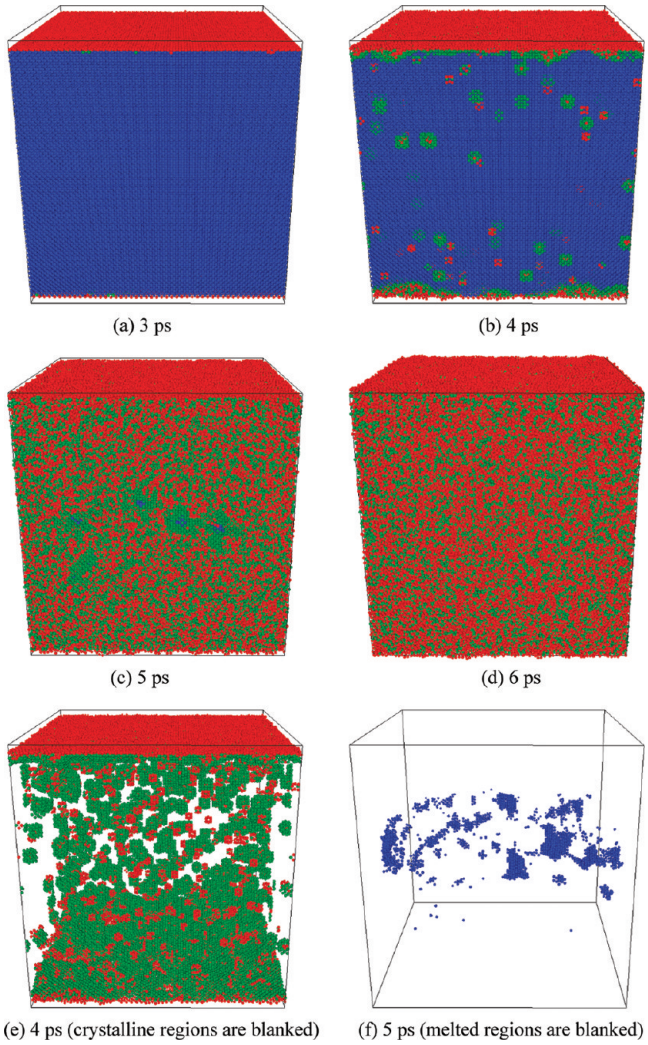


**Figure 5.** Snapshots of atomic configurations during the melting process in a 20 nm single crystal Au film irradiated with a 200 fs laser pulse at an absorbed fluence of 180 J/m$^2$. The snapshots are shown for times of 3 ps (a), 4 ps (b, e), 5 ps (c, f), and 6 ps (d) after the laser pulse. The coloring scheme is the same as in Figure 1; blue atoms have local crystalline surroundings, and red and green atoms belong to the liquid phase. In part e, the atoms in the crystalline parts of the film ($\Phi < 0.1$) are blanked to provide a clear view of the emerging point defects and disordered regions. In part f, the atoms that belong to the liquid parts of the film ($\Phi > 0.1$) are blanked to expose the remaining crystalline regions.

At a fluence of 45 J/m$^2$, the lattice temperature exceeds the equilibrium melting temperature at 9 ps, reaches the maximum value of $1.16T_m$ by a time of ~20 ps, and gradually decreases and saturates at $T_m$ at later times, Figure 4c and d. The decrease of the temperature corresponds to the melting of the film that proceeds in this case by the propagation of two melting fronts from the free surfaces of the film, Figure 6. The velocity of the melting fronts decreases from the maximum value of ~100 m/s at the time when the temperature of the film is at its maximum down to zero as the temperature approaches the equilibrium melting temperature. The final state of the system at the end of the simulation is a partially melted film with a crystalline layer located in the middle of the film. The fraction of the film that remains in the crystalline form, $\alpha$, can be predicted by balancing the amount of energy deposited by the laser pulse with the energy needed for heating the film from 300 K to $T_m$ and subsequent melting of the $(1 - \alpha)$ fraction of the film:

$$F_{abs} = (\int_{300}^{T_m} C_l(T)\,dT + \int_{300}^{T_m} C_e(T)\,dT)L + \Delta H_m L(1 - \alpha) \quad (3)$$

where $F_{abs}$ is the absorbed fluence, $L$ is the thickness of the film, $C_l$ and $C_e$ are the lattice and electron heat capacities, $\Delta H_m$ is the heat of melting, and a minor correction related to the interfacial energies is neglected. Using parameters of the EAM Au material given in ref 38 and the temperature dependence of the electron heat capacity from ref 43, the fraction of the crystalline part of the film can be estimated to be $\alpha = 0.53$ at $F_{abs} = 45$ J/m$^2$. This estimation is consistent with the results of the simulations, where about half of the atoms in the atomic configuration shown for 500 ps in Figure 6 belong to the crystalline part of the film.

Thermally activated generation of vacancy−interstitial pairs, discussed above for the simulation performed at 180 J/m$^2$, is also observed at 45 J/m$^2$, although the number of point defects is much smaller at this lower laser fluence. In particular, 9 vacancy−interstitial pairs are identified in the crystalline part of the target at 100 ps, with the number of point defects changing to 11 vacancies and 8 interstitials at 200 ps and 10 vacancies and 3 interstitials at 500 ps. The fast decrease in the number of interstitials with time is related to their high mobility. The active diffusion of the interstitials allows them to escape to the liquid−crystal interfaces, leaving the vacancies behind. A similar process of the laser-induced generation of a high concentration of vacancies was recently observed in simulations performed for a bulk Cr target.[31]

**3.3. Laser Melting of Nanocrystalline Films.** The results of the simulations performed for nanocrystalline films irradiated at laser fluences of 45 and 180 J/m$^2$ are illustrated in Figures 7−9. At a fluence of 180 J/m$^2$, the evolution of the average electron and lattice temperatures of the film (Figure 7a and b)

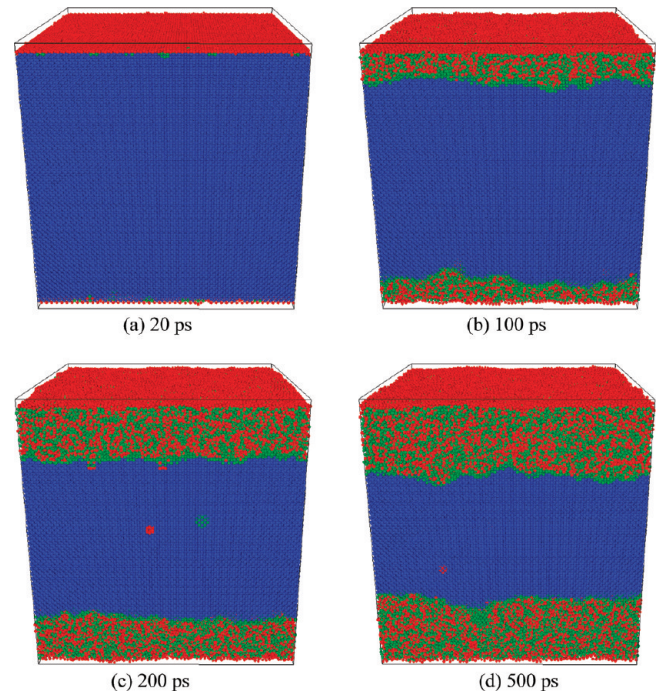


**Figure 6.** Snapshots of atomic configurations during the melting process in a 20 nm single crystal Au film irradiated with a 200 fs laser pulse at an absorbed fluence of 45 J/m$^2$. The snapshots are shown for times of 20 ps (a), 100 ps (b), 200 ps (c), and 500 ps (d) after the laser pulse. The coloring scheme is the same as in Figure 1; blue atoms have local crystalline surroundings, and red and green atoms belong to the liquid phase.

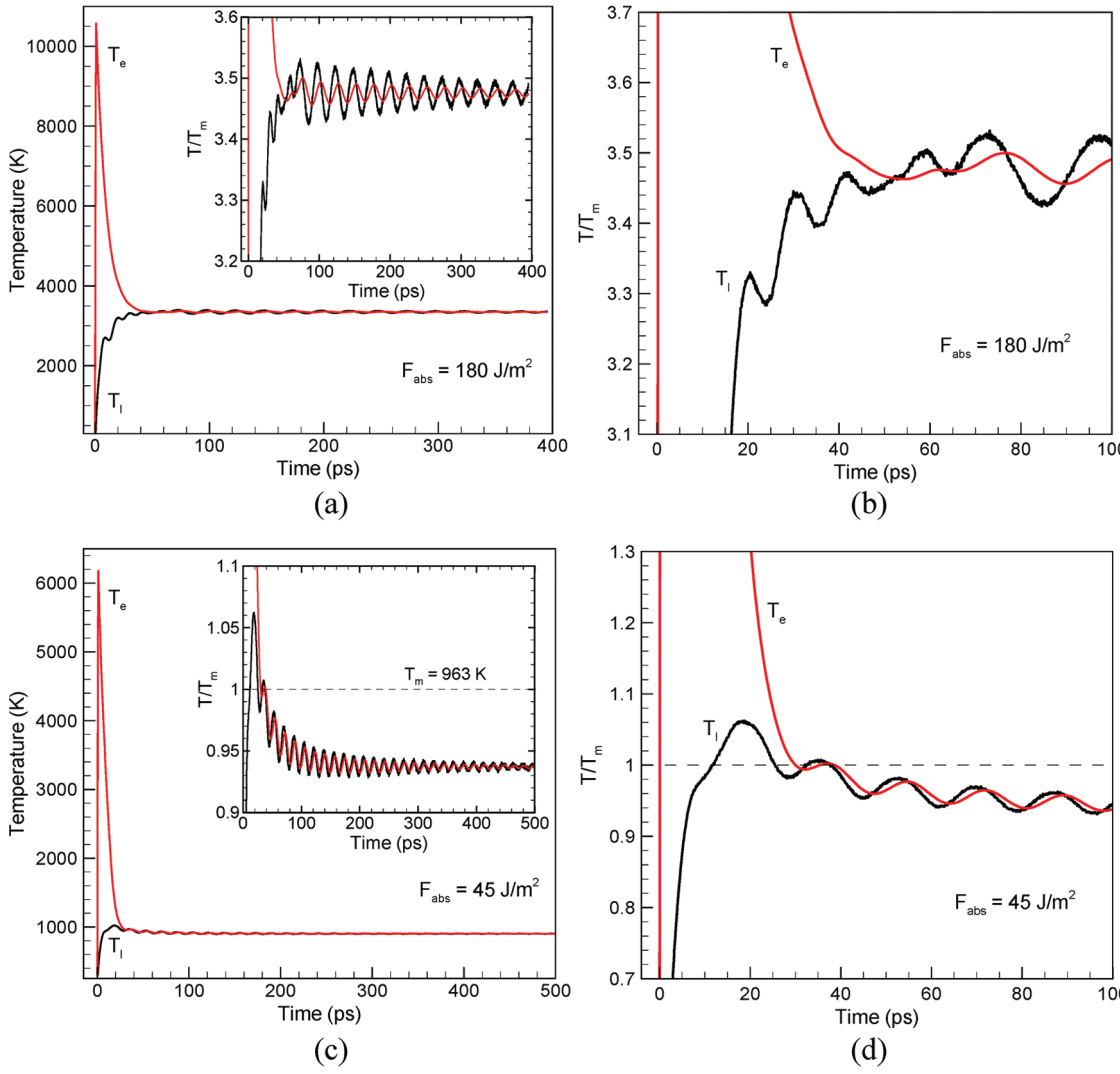


**Figure 7.** Temporal evolution of the average electron and lattice temperatures, $T_e$ and $T_l$, obtained in TTM-MD simulations of nanocrystalline Au films irradiated by 200 fs laser pulses at absorbed fluences of 180 J/m$^2$ (a,b) and 45 J/m$^2$ (c,d). The horizontal dashed lines in panels c and d mark the equilibrium melting temperature of the EAM Au, $T_m$. In panels b and d and in the insets in panels a and c, the temperature is normalized by the equilibrium melting temperature, and the scale is chosen to show a closer view of the evolution of the electron and lattice temperatures during and after the melting process.

is similar to the one observed for the single crystal film (Figure 4a and b), except for the somewhat smaller amplitude of the temperature oscillations observed for the nanocrystalline film. Snapshots of atomic configurations shown in Figure 8 suggest that grain boundary melting at the early stage of the heating process makes some initial contribution to the initiation of the melting process in the case of the nanocrystalline film. Indeed, the broadening of the disordered regions around the grain boundaries has made a much more substantial contribution to the increase in the amount of material melted by the time of 4 ps (Figure 8b) as compared to the propagation of the melting fronts from the two free surfaces of the single crystal film (Figure 5b and e). Nevertheless, the overall time scales of the melting process observed for the two films are similar in this high fluence regime (Figure 10a) and are largely defined by the fast increase in the lattice temperature. In both simulations, the lattice temperature exceeds the limit of crystal stability against the homogeneous melting ($\sim$1.25$T_m$) by a time of $\sim$2 ps, leading to the rapid disappearance of the crystalline regions remaining in the film within the next 3 ps (Figures 5f and 8d).

The effect of the nanocrystalline structure of the film on the melting process is much stronger at low fluences, where significant qualitative differences in the mechanisms of melting and the final phase composition of the irradiated films are observed. The differences in the melting process are apparent from the comparison between the lattice temperature profiles shown in Figures 4c,d and 7c,d for the two simulations performed at the same laser fluence of 45 J/m$^2$. The maximum lattice temperature reached by the time of 20 ps is smaller in the case of the nanocrystalline film, which can be explained by the early onset of the grain boundary melting that converts a part of the thermal energy to the heat of melting of the grain boundary regions. Indeed, an extensive melting of the grain boundary regions is apparent from the snapshot of the atomic configuration shown for a time of 20 ps in Figure 9a. The temperature of the nanocrystalline film drops below the equilibrium melting temperature within the next 10 ps (Figure 7d) and continues to decrease until a time of $\sim$150 ps (Figure 7c). The temperature eventually saturates at a level that is $\sim$6% below the equilibrium melting temperature. This temperature evolution is in sharp contrast with the one observed for the single crystal film, where the temperature slowly decreases with time and approaches the equilibrium melting temperature at $\sim$500 ps, Figure 4c.

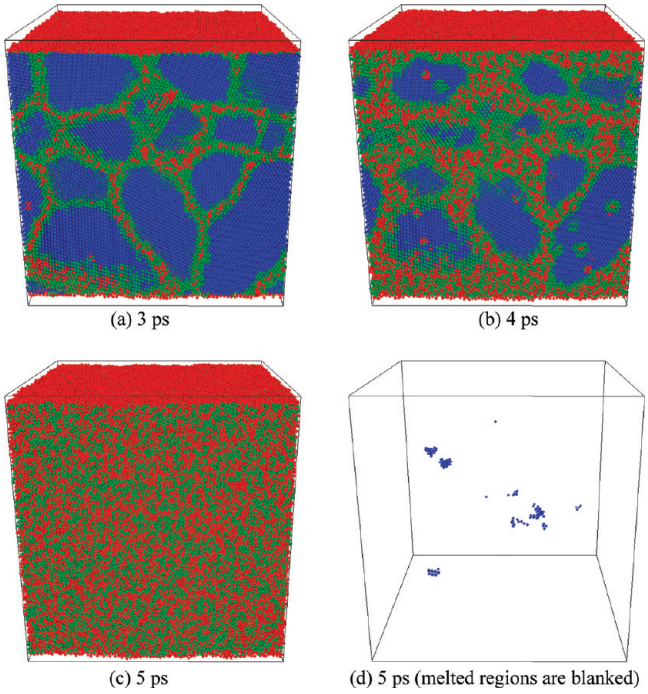


**Figure 8.** Snapshots of atomic configurations during the melting process in a 20 nm nanocrystalline Au film irradiated with a 200 fs laser pulse at an absorbed fluence of 180 J/m$^2$. The snapshots are shown for times of 3 ps (a), 4 ps (b), and 5 ps (c,d) after the laser pulse. The coloring scheme is the same as in Figure 1; blue atoms have local crystalline surroundings, and red and green atoms belong to the liquid phase. In part d, the atoms that belong to the liquid parts of the film ($\Phi > 0.1$) are blanked to expose the remaining crystalline regions.

The temperature evolution shown in Figure 7c and d can be related to the structural changes in the irradiated nanocrystalline film that are illustrated by the snapshots shown in Figure 9. The initial melting of the grain boundary regions proceeds under conditions of overheating above the equilibrium melting temperature and, by the time of 50 ps, generates a mixed liquid−crystal system in which crystalline grains (or clusters) are surrounded by the melted material (Figure 9e). At this time of 50 ps, the temperature of the film is already below the equilibrium melting temperature (Figure 7d). Nevertheless, the melting process continues, as evidenced by the shrinkage of the crystalline clusters (Figure 9e−h) and the decrease in the total number of atoms in the crystalline parts of the system (Figure 10b). The last crystalline region present at 200 ps (Figure 9h) disappears by a time of 250 ps. The explanation of the melting of the crystalline clusters occurring under conditions of undercooling below the equilibrium melting temperature is provided below, in section 3.4, where a quantitative analysis of the stability of small solid clusters surrounded by liquid is performed within the classical nucleation theory.

The structural changes in the nanocrystalline film irradiated with a short laser pulse can be further investigated through examination of the evolution of the reduced pair distribution function $G(r)$ and the corresponding structure function $S(Q)$ calculated for the transient atomic configurations generated in the simulation performed at 45 J/m$^2$ and shown in Figure 11. The equations defining the functions and the numerical methods used for calculation of $G(r)$ and $S(Q)$ from atomic configurations are presented in ref 38. Before the laser irradiation, at 0 ps, both functions exhibit distinct peaks characteristic of the fcc crystalline structure. Following the laser excitation, the fast temperature increase and the onset of the melting process result in broadening of the peaks in $G(r)$ and reduction of their

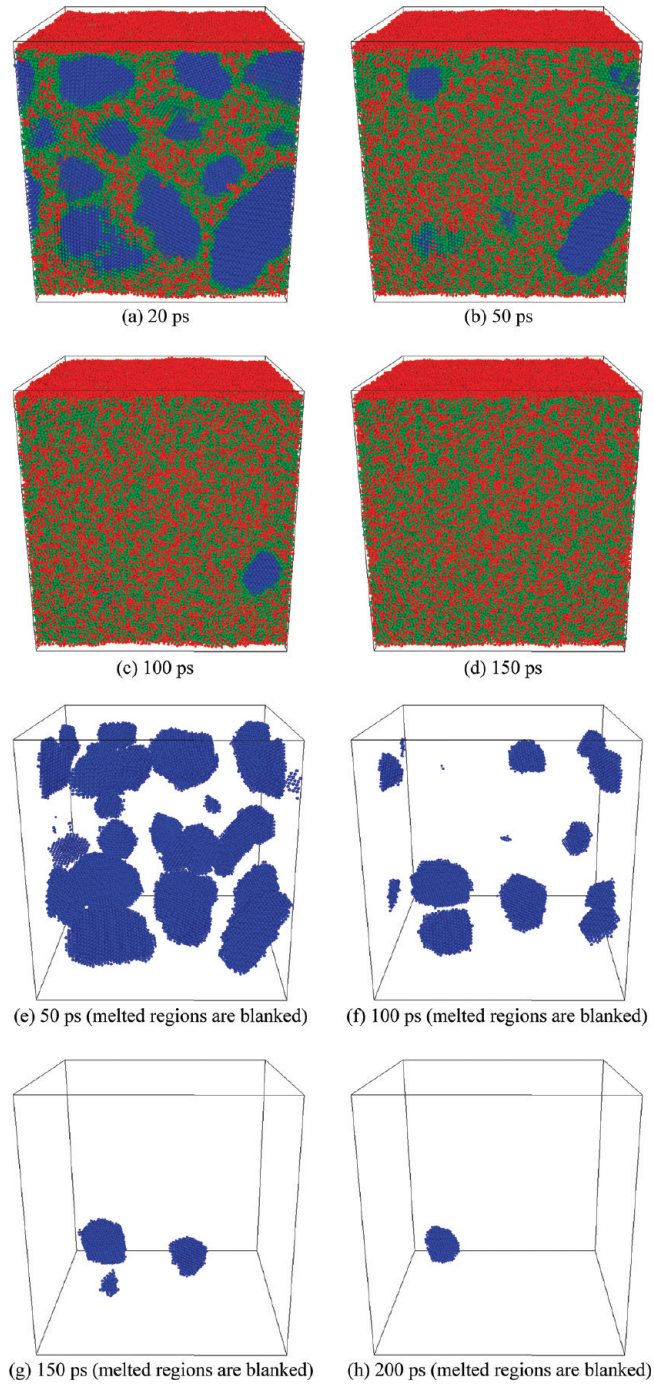


**Figure 9.** Snapshots of atomic configurations during the melting process in a 20 nm nanocrystalline Au film irradiated with a 200 fs laser pulse at an absorbed fluence of 45 J/m$^2$. The snapshots are shown for times of 20 ps (a), 50 ps (b,e), 100 ps (c,f), 150 ps (d,g), and 200 ps (h) after the laser pulse. The coloring scheme is the same as in Figure 1; blue atoms have local crystalline surroundings, and red and green atoms belong to the liquid phase. In parts e−h, the atoms that belong to the liquid parts of the film ($\Phi > 0.1$) are blanked to expose the remaining crystalline regions.

intensities. At 20 ps, when analysis based on the centrosymmetry parameter indicates that ∼46% of atoms still have local crystalline surroundings, some of the crystalline peaks in $G(r)$ are completely obscured and cannot be identified, e.g., the peak corresponding to the second-neighbor shell in the fcc structure (Figure 11a). The disappearance of this and other peaks, however, does not imply the complete absence of the crystalline ordering in the system. As shown in the analysis reported in

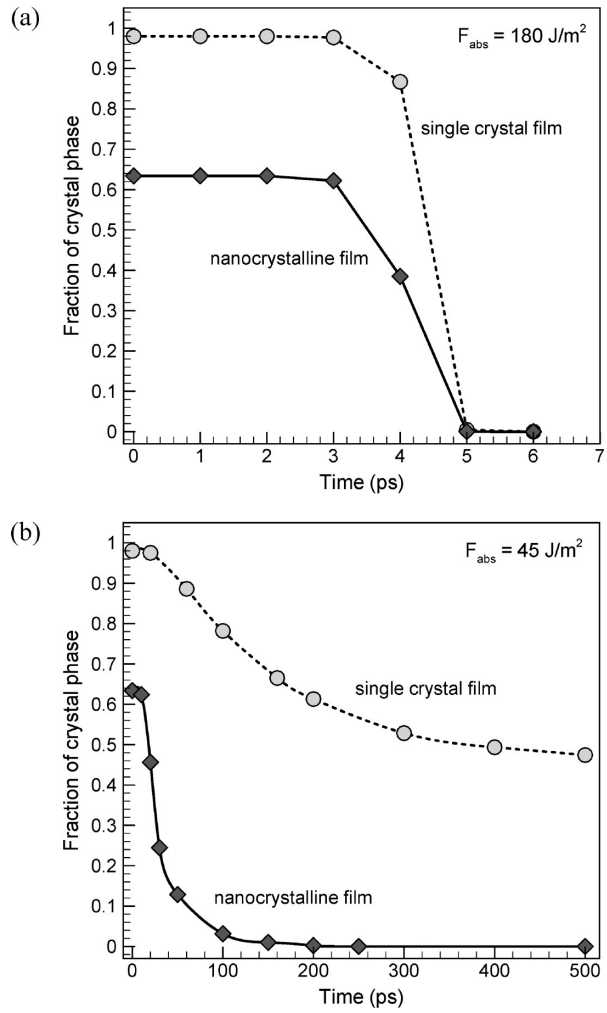


**Figure 10.** Time evolution of the fraction of atoms in the crystalline parts of the single crystal (dashed lines) and nanocrystalline (solid lines) films irradiated with 200 fs laser pulses at absorbed fluences of 180 J/m$^2$ (a) and 45 J/m$^2$ (b). The atoms in the crystalline parts of the films are identified by the value of the centrosymmetry parameter ($\Phi < 0.1$). The fractions of the crystal phase are not equal to unity at the initial time of 0 ps due to the contribution of atoms at the free surfaces of the film and in the grain boundary regions.

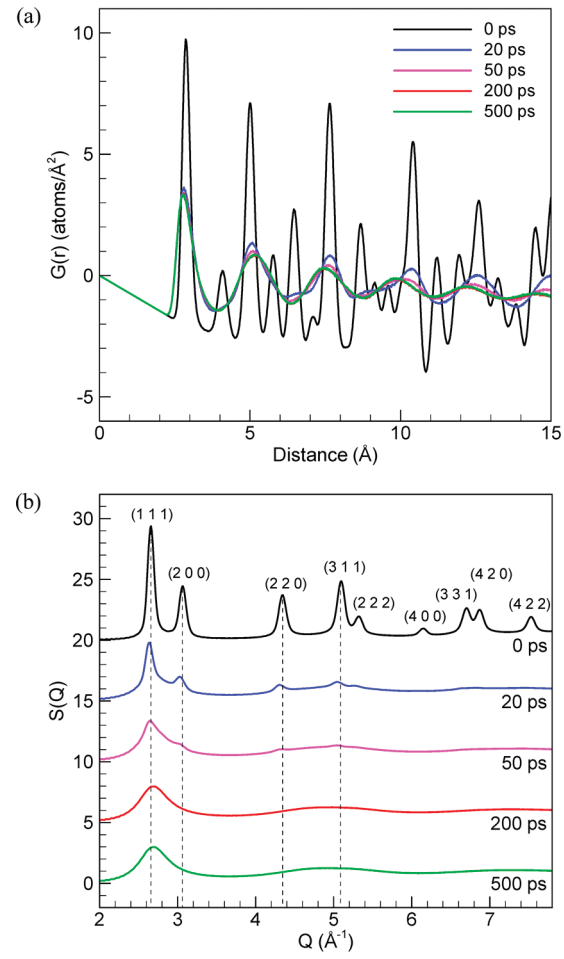


**Figure 11.** Reduced pair distribution functions $G(r)$ (a) and structure functions $S(Q)$ (b) computed for atomic configurations obtained in a TTM-MD simulation of a 20 nm nanocrystalline Au film irradiated with a 200 fs laser pulse at an absorbed fluence of 45 J/m$^2$. The functions are calculated for times of 0, 20, 50, 200, and 500 ps after the laser pulse.

ref 38, some of the peaks can become completely obscured by the broadening of all of the peaks due to the increased amplitude of atomic vibrations at a high temperature. The shape of $G(r)$ calculated at 20 ps still has some features that can be attributed to the crystalline arrangement of atoms in the remaining solid parts of the system. The crystalline features become almost unidentifiable in $G(r)$ calculated at 50 ps, when the crystalline clusters account for ~13% of atoms in the system, and completely disappear by 200 ps, when the only remaining crystalline cluster shown in Figure 9h is composed of 1168 atoms (0.2% of the total number of atoms).

The identification of the remaining crystalline regions at the late stages of the melting process appears to be more straightforward from the analysis of the structure factor, $S(Q)$, which can be related[38] to the diffraction profiles measured in time-resolved X-ray and electron diffraction experiments.[17,19−24,26,72−74] While the heights of all of the diffraction peaks decrease sharply during the first tens of picoseconds due to the increasing thermal vibrations of the atoms (Debye−Waller factor)[53] and the progressing melting process, the peaks characteristic of the fcc structure can still be identified in $S(Q)$ plotted for 20 and 50 ps, Figure 11b. The positions of the diffraction peaks at these times are shifted to the left with respect to the positions of the peaks before the irradiation, at 0 ps. Similar shifts of the peaks have been observed in earlier simulations of laser heating and melting performed for single crystal films,[38,39] where the shifts have been attributed to the uniaxial expansion of the film in the direction perpendicular to the free surfaces in response to the laser heating. In addition to the shifts of the peaks, the structure factor calculated for the single crystal films also exhibited splitting of some of the peaks due to the transformation of the cubic lattice to the tetragonal one upon the uniaxial expansion.[38,39] In the case of the nanocrystalline structure of the film, however, the random crystallographic orientations of grains ensures that the uniaxial expansion equally affects interplanar distances in all crystallographic directions and no splitting of the peaks is observed. The peaks characteristic of the fcc structure disappear completely, and $S(Q)$ takes the shape characteristic of the liquid structure by the time of 200 ps, when the fraction of the crystalline phase in the system becomes 0.2 at. %.

**3.4. Thermodynamic Analysis of Clusters in Undercooled Liquid.** The drastic difference in the melting behavior of single crystal and nanocrystalline films irradiated at the same laser fluence of 45 J/m$^2$ calls for further analysis of the melting conditions. The difference between the partial heterogeneous melting of about a half of the film in the case of the single crystal film and the complete melting of the nanocrystalline film

cannot be attributed solely to the higher initial energy density in the nanocrystalline film associated with the energy of the grain boundaries. The difference in the potential energy densities in the two films is 0.022 eV/atom (2.1 kJ $mol^{-1}$) which corresponds to 25% of the enthalpy of melting ($\Delta H_m = 8.4$ kJ $mol^{-1}$).[38] Thus, the contribution from the energy of the grain boundaries cannot explain the melting of ~50% part of the film that remains crystalline at the end of the simulation performed for the single crystal film, Figure 6d. To explain the complete melting of the nanocrystalline layer at a fluence of 45 J/$m^2$, below, we provide a simple thermodynamic analysis of the melting conditions in the nanocrystalline film.

The snapshots of atomic configurations shown in Figure 9 indicate that the initiation of the melting process at grain boundaries results in the separation of the crystalline domains by liquid regions. Therefore, the remaining part of the melting process can be described as dissolution of individual crystalline clusters in the liquid. The condition for the equilibrium between a crystalline cluster and a surrounding liquid can be found following the analysis of the classical nucleation theory that considers the Gibbs free energy change upon the formation of a spherical solid nucleus of radius $r$ in an undercooled liquid:[77]

$$\Delta G_r = -\frac{4}{3}\pi r^3 \Delta G_v + 4\pi r^2 \gamma_{SL} \quad (4)$$

where $\Delta G_v$ is the Gibbs free energy difference between the solid and liquid phases per unit volume and $\gamma_{SL}$ is the solid−liquid interfacial free energy. For small undercoolings, $\Delta T = T_m - T$, the difference in the specific heats of the solid and liquid phases can be neglected and $\Delta G_v$ can be approximated by $\Delta H_m \Delta T / T_m$, with $\Delta H_m$ expressed in units of energy per volume. For a given undercooling $\Delta T$, the critical size of a solid cluster that corresponds to the state of unstable equilibrium between the cluster and the surrounding liquid can be then obtained from eq 4 and expressed through $\gamma_{SL}$ and $\Delta H_m$:

$$r^* = \frac{2\gamma_{SL}}{\Delta G_v} = \left(\frac{2\gamma_{SL} T_m}{\Delta H_m}\right)\frac{1}{\Delta T} \quad (5)$$

For $r < r^*$, the solid cluster is thermodynamically unstable, as dissolution of the cluster would lower the free energy of the system, whereas for $r > r^*$ the free energy of the system would decrease if the cluster grows. For a cluster of a particular radius $r$, the condition given by eq 5 can be reformulated to give the critical undercooling temperature $T^*$ that corresponds to the equilibrium between the cluster and the surrounding liquid

$$T^* = T_m\left[1 - \frac{2\gamma_{SL}}{\Delta H_m}\frac{1}{r}\right] \quad (6)$$

Similar to the discussion of the critical radius, the decrease of the free energy corresponds to the dissolution of the cluster at $T > T^*$ and growth of the cluster at $T < T^*$, indicating that $T^*$ corresponds to the state of unstable equilibrium between the cluster of radius $r$ and the surrounding liquid. The temperature given by eq 6 has also been interpreted in ref 2 as an upper limit of the melting temperature of a small particle with radius $r$.

In order to relate the cluster size dependence of the critical undercooling temperature given by eq 6 to the results of the laser melting simulations, it is necessary to determine the solid−liquid interfacial free energy for the EAM Au material. A number of computational approaches have been developed for calculation of the solid−liquid interfacial free energy.[79−84] Using the capillary fluctuation method described in refs 81−83, we evaluated the interfacial free energies for three interfaces, (100), (110), and (210), to be 104, 100, and 102 mJ/$m^2$, respectively. We did not perform calculations for the (111) interface, which can be expected to have the lowest value of the free energy.[80,81,84] The small difference between the (100) and (110) interfaces and the ordering of $\gamma_{SL}^{100} > \gamma_{SL}^{110}$ is consistent with most of the earlier calculations performed with Lennard-Jones and EAM potentials.[80−84] The values of the interfacial free energy, however, are smaller than the experimental value of 132 mJ/$m^2$ obtained from measurements of the frequency of homogeneous nucleation in small droplets of supercooled Au,[85] as well as the value of ~126 mJ/$m^2$ calculated with the capillary fluctuation method for Voter-Chen EAM Au.[83]

The relatively low values of the interfacial free energy predicted in our calculations can be partially attributed to the lower value of the melting temperature of Johnson EAM Au, 963 K, as compared to 1120 K of Voter-Chen EAM Au and the experimental value of 1338 K. The variation of the interfacial energy with melting temperature can be described by Turnbull's empirical relationship,[85] $\gamma = \alpha T_m \Delta S_m \rho^{2/3}$, where $\Delta S_m$ is the entropy change upon melting, $\rho$ is the number density of the solid phase, and $\alpha$ is the so-called Turnbull coefficient that has a relatively small variation for different metals.[84−86] Since the values of $\Delta S_m$ in many close-packed metals are close to each other, the Turnbull relationship implies an approximately linear dependence of the interfacial free energy on the melting temperature. Accounting for the lower melting temperature of Johnson EAM Au (14% difference with Voter-Chen EAM Au and 28% difference with the experimental value) brings the interfacial energies predicted in our capillary fluctuation method calculations closer to the values reported in the literature.

An alternative approach to finding the interfacial free energy and the critical undercooling temperature has been recently suggested and applied for a Lennard-Jones system in ref 87. This approach is based on direct analysis of the stability of a solid cluster of radius $r$ thermally equilibrated with surrounding undercooled liquid in constant pressure−constant temperature MD simulations. By performing simulations at different temperatures, the critical undercooling temperature is identified as the temperature at which the cluster does not show clear trends for growth ($T < T^*$) or dissolution ($T > T^*$). After the critical undercooling temperature is determined for several different radii, the effective orientationally averaged interfacial free energy of the cluster can be found by fitting the data to eq 6. This approach is particularly suitable for interpretation of the results of the laser melting simulations, since the value of the effective interfacial free energy of the cluster naturally accounts for the contributions from interfaces of different crystallographic orientations as well as for any spontaneous faceting of the clusters.

The calculation of the critical undercooling temperature for the Johnson EAM Au potential used in this work is illustrated in Figure 12. The initial configuration of a crystalline cluster embedded in an undercooled liquid is created as follows. A spherical region of radius $r$ is first defined within an initial MD computational cell represented by an fcc crystal with dimensions of 9.1 × 9.1 × 9.1 $nm^3$ or 16.6 × 16.6 × 16.6 $nm^3$ (this larger computational cell is used in simulations performed for the largest crystalline cluster with a radius of 4.3 nm). The temperature outside the spherical region is then increased well above the equilibrium melting temperature to induce melting while keeping the temperature inside the spherical region below the equilibrium melting temperature, so that the spherical region remains in the solid state. Following the complete melting of the material outside the spherical cluster, the temperatures of

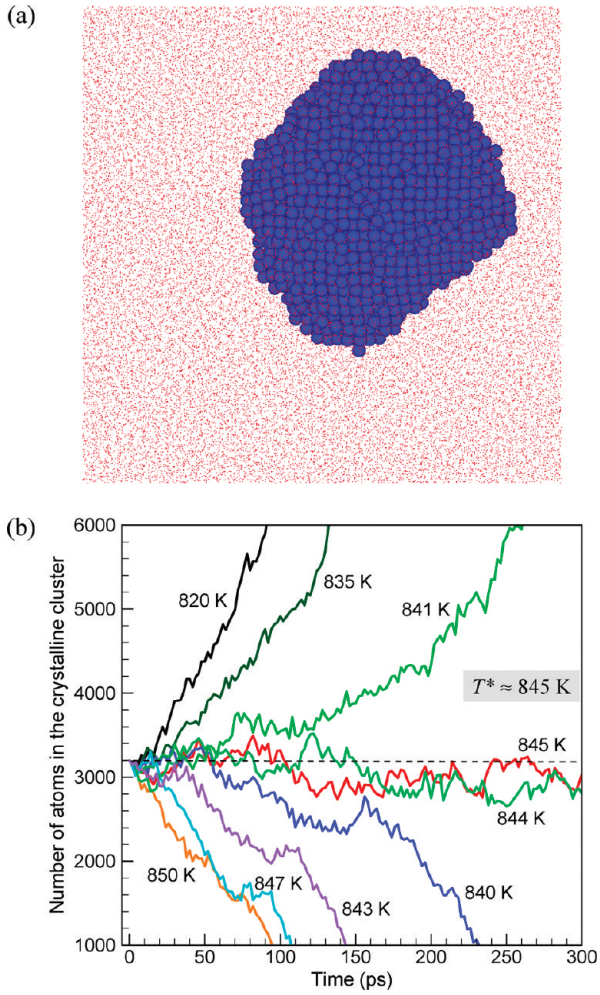


**Figure 12.** Snapshot of an atomic configuration used in the investigation of the stability of solid clusters surrounded by undercooled liquid (a) and the time evolution of the number of atoms in the crystalline cluster in MD simulations performed at different temperatures (b). The data is shown for one of the clusters used in the simulations (the initial radius is 2.4 nm, and the number of atoms is 3198). The atoms in the crystal are distinguished from the ones in the liquid phase on the basis of the local order parameter. In part a, the atoms in the cluster are shown by blue spheres, and the atoms in the surrounding liquid are shown by red dots.

the solid cluster and the surrounding liquid are brought to the same designated value below the equilibrium melting temperature by the Berendsen thermostat method[88] applied separately to the two parts of the system. The simulations are performed at a constant zero pressure and periodic boundary conditions imposed in all three directions. The procedure described above produces a thermally equilibrated system consisting of a solid cluster surrounded by an undercooled liquid. A snapshot of a typical atomic configuration is shown in Figure 12a for a cluster with a radius of ~2.4 nm (3198 atoms). It can be seen that the equilibrated solid cluster exhibits substantial deviations from the original spherical shape due to the faceting that reduces the total interfacial energy in the liquid-cluster system.

Following the initial equilibration, the system is allowed to evolve under constant temperature and constant pressure conditions for 300 ps. The atoms with local crystalline surroundings are identified by calculating the local order parameter,[34,38,57] and the number of atoms in the crystalline cluster is monitored during the simulations. The procedure of identification of the critical undercooling temperature is illustrated in Figure 12b for a crystalline cluster with an initial radius of 2.4 nm. At

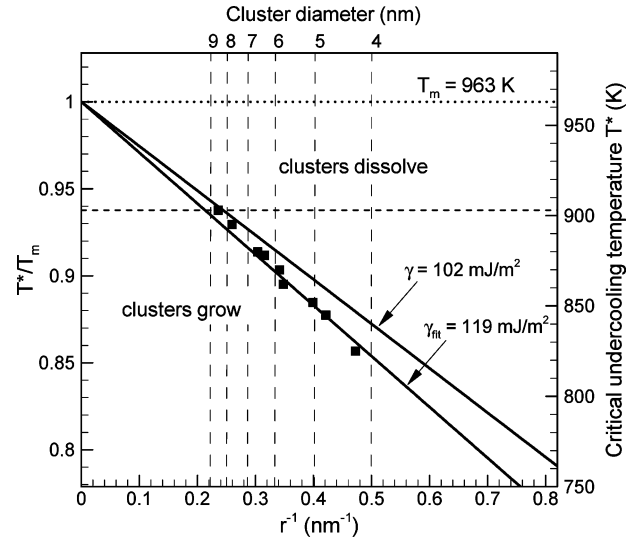


**Figure 13.** The critical undercooling temperature of a crystalline cluster surrounded by undercooled liquid as a function of the size of the cluster. The data points are obtained in MD simulations of the evolution of clusters surrounded by liquid at different undercoolings, as described in the text and illustrated in Figure 12. The solid lines show the predictions of eq 6 with the values of interfacial free energies predicted with the capillary fluctuation method ($\gamma$ = 102 mJ/m$^2$) and obtained by fitting eq 6 to the data points ($\gamma_{fit}$ = 119 mJ/m$^2$). The horizontal dotted line shows the equilibrium melting temperature of EAM Au. The horizontal dashed line marks the maximum level of undercooling observed in the simulation of laser melting of nanocrystalline film irradiated at a fluence of 45 J/m$^2$.

temperatures of 820 and 835 K, the size of the cluster increases rapidly, leading to the complete solidification of the computational cell on the time scale of the simulation. At temperatures of 850 and 847 K, the size of the cluster shrinks and the cluster dissolves. At temperatures of 845 and 844 K, the size of the cluster fluctuates around the initial value for the duration of the simulation. This behavior is consistent with the condition of equilibrium between the crystalline cluster and the surrounding liquid, and therefore, we estimate the critical undercooling temperature for this cluster to be 895 K. Note that the equilibrium between the cluster of the critical size and the surrounding liquid is an unstable one and structural fluctuations can easily destabilize the fragile cluster−liquid coexistence, triggering either growth or dissolution of the cluster. Indeed, in three simulations performed slightly below the estimated critical undercooling temperature, we observe either growth (at 841 K) or dissolution (at 840 and 843 K) of the cluster. This observation highlights the stochastic nature of the structural fluctuations around the critical undercooling temperature. The number of simulations performed for each size of crystalline cluster is chosen to be sufficiently large to ensure the accuracy of the estimation of the values of the critical undercooling temperature to be within several degrees K.

The results of the calculation of the critical undercooling temperature for clusters of different sizes are shown in Figure 13. The values of the critical undercooling temperature follow a linear dependence on the inverse of the cluster radius predicted by eq 6. Fitting eq 6 to the data points yields a value of the effective interfacial free energy of 119 mJ/m$^2$. Taking into account that this interfacial free energy has contributions from different crystallographic facets present in the clusters and that the shapes of the clusters can have significant deviation from the spherical shape assumed in the model, the predicted value can be considered to be in a reasonable agreement with the

values of 100−104 mJ/m$^2$ obtained for the (100), (110), and (210) interfaces using the capillary fluctuation method. We note, however, that calculations of the critical undercooling temperature for the Lennard-Jones system reported in ref 87 yielded a value of the effective interfacial energy of small solid clusters that is smaller than the values of interfacial energies of flat interfaces predicted for the same system with the capillary fluctuation method.[79−81] These contradicting results call for a more detailed analysis of the factors affecting the computational predictions of the two methods used in the evaluation of the interfacial free energy.

The observation of the strong size dependence of the thermal stability of a solid cluster surrounded by an undercooled liquid can be directly applied for interpretation of the results of the simulation of laser melting of the nanocrystalline film at 45 J/m$^2$. As can be seen from Figure 7c and d, the temperature of the film exceeds the equilibrium melting temperature at 12 ps, goes down below the melting temperature by ∼25 ps, decreases below $0.95T_m$ by ∼100 ps, and saturates at a level of $\sim 0.94T_m$ (∼903 K) at a later time. At the time when the temperature of the film drops below the melting temperature, the structure of the system can already be described as a group of crystalline clusters surrounded by liquid. The analysis of the cluster stability, therefore, can be based on the plot of the cluster size dependence of the critical undercooling temperature shown in Figure 13. The level of the maximum undercooling observed in the simulation is shown by the dashed line in Figure 13. At this undercooling, all clusters with a diameter less than ∼9.5 nm (calculated from eq 6 with $\gamma_{fit} = 119$ mJ/m$^2$) are unstable and their dissolution would reduce the free energy of the system. Although the diameter of the largest grain present in the initial system exceeds 10 nm (see inset in Figure 2), by the time of 100 ps, the remaining solid clusters are all smaller than ∼5 nm and are well below the critical size. Therefore, the continuation of the melting process below the equilibrium melting temperature can be explained by the subcritical size of the crystalline clusters, which results in their gradual dissolution.

## 4. Conclusions

The effect of the high density of grain boundaries in nanocrystalline metals on the characteristics of the melting process induced by short pulse laser irradiation is investigated in atomistic simulations performed for single crystal and nanocrystalline Au films. The simulations are performed with a hybrid atomistic-continuum model that combines the classical MD method with a continuum-level description of the laser excitation and subsequent relaxation of the conduction band electrons. A description of the electron temperature dependence of the thermophysical properties of Au that accounts for the contribution of the thermal excitation of electrons from states located below the Fermi level is incorporated into the model and is found to play a major role in defining the kinetics of the melting process. Compared with the results of earlier simulations performed for single crystal films with conventional assumptions of a linear temperature dependence of the electron heat capacity and a constant value of the electron−phonon coupling, the simulations performed with the new temperature dependences of the thermophysical parameters of the material predict a significant, by more than a factor of 2, decrease in the time of the onset of the melting process at high laser fluences. The inclusion of the contribution from the thermal excitation of the lower band electrons into the model is found to be essential for bringing the computational predictions into quantitative agreement with the results of time-resolved experimental probing of the laser-induced structural transformations.

A detailed analysis of the effect of the nanocrystalline structure on the kinetics and mechanisms of melting indicates that at all laser fluences the melting process starts from the grain boundary regions as soon as the lattice temperature approaches and exceeds the equilibrium melting temperature. The contribution of the grain boundary melting to the overall melting process is, however, very different in the low fluence regime (below or close to the threshold for the complete melting of the film) and in the high fluence regime (significantly above the melting threshold).

At high laser fluences, the temperatures of both single crystal and nanocrystalline films quickly exceed the limit of thermal stability of the crystal lattice, resulting in a rapid collapse of the crystal structure within the next several picoseconds. The onset of the homogeneous melting is preceded by thermally activated generation of a large number of vacancy−interstitial pairs that introduce localized lattice distortions and reduce the stability of the crystal structure against melting. Although the grain boundary melting in nanocrystalline films results in a certain decrease in the size of the crystalline grains at the initial stage of the laser heating, the overall time scale of the melting process is largely defined by the fast temperature increase and the rapid homogeneous nucleation and growth of disordered region throughout the overheated crystalline parts of the films.

At lower laser fluences, when the maximum lattice temperature does not exceed the limit of crystal stability against homogeneous melting, the microstructure of the film is found to have a much stronger effect on the characteristics of the melting process. In particular, in two simulations performed at the same absorbed fluence of 45 J/m$^2$, a partial melting of about a half of a 20 nm single crystal Au film and a complete melting of a nanocrystalline film of the same size are observed. The melting of the single crystal film proceeds by propagation of the melting fronts from the free surfaces of the film and the system reaches an equilibrium state when the temperature of the film drops down to the equilibrium melting temperature. In the case of the nanocrystalline film, the melting continues below the equilibrium melting temperature and the last crystalline regions disappear under conditions of about 6% undercooling below the melting temperature. The unusual melting behavior of the nanocrystalline films is explained on the basis of thermodynamic analysis of the stability of small crystalline clusters surrounded by undercooled liquid.

**Acknowledgment.** The authors thank Dr. Ralph Ernstorfer of the Max Planck Institute of Quantum Optics, Garching, Germany, for the initial discussion that led to this study. Financial support of this work is provided by the NSF through Awards CTS-0348503 and DMR-0907247. One of the authors (Z.L.) is also supported by the NSF sponsored Renewable Energy Materials Research Science and Engineering Center (REMRSEC) at the Colorado School of Mines.

## References and Notes

(1) Frenkel, J. *Kinetic Theory of Liquids*; Clarendon: Oxford, U.K., 1946.
(2) Couchman, P. R.; Jesser, W. A. *Nature (London)* **1977**, *269*, 481–483.
(3) van der Veen, J. F. *Surf. Sci.* **1999**, *433−435*, 1–11.
(4) Dash, J. G. *Rev. Mod. Phys.* **1999**, *71*, 1737–1743.
(5) Lutsko, J. F.; Wolf, D.; Phillpot, S. R.; Yip, S. *Phys. Rev. B* **1989**, *40*, 2841–2855.
(6) Cahn, R. W. *Nature (London)* **1986**, *323*, 668–669.
(7) Daeges, J.; Gleiter, H.; Perepezko, J. H. *Phys. Lett. A* **1986**, *119*, 79–82.
(8) Gråbæk, L.; Bohr, J.; Andersen, H. H.; Johansen, A.; Johnson, E.; Sarholt-Kristensen, L.; Robinson, I. K. *Phys. Rev. B* **1992**, *45*, 2628–2637.

(9) Sheng, H. W.; Ren, G.; Peng, L. M.; Hu, Z. Q. *Philos. Mag. Lett.* **1996**, *73*, 179–186.
(10) Zhang, L.; Jin, Z. H.; Zhang, L. H.; Sui, M. L.; Lu, K. *Phys. Rev. Lett.* **2000**, *85*, 1484–1487.
(11) Lindemann, F. A. *Phys. Z.* **1910**, *11*, 609–612.
(12) Born, M. *J. Chem. Phys.* **1939**, *7*, 591–603.
(13) Kuhlmann-Wilsdorf, D. *Phys. Rev.* **1965**, *140*, A1599–A1610.
(14) Wang, J.; Li, J.; Yip, S.; Phillpot, S.; Wolf, D. *Phys. Rev. B* **1995**, *52*, 12627–12635.
(15) Rethfeld, B.; Sokolowski-Tinten, K.; von der Linde, D.; Anisimov, S. I. *Phys. Rev. B* **2002**, *65*, 092103.
(16) Ivanov, D. S.; Zhigilei, L. V. *Phys. Rev. Lett.* **2007**, *98*, 195701.
(17) Williamson, S.; Mourou, G.; Li, J. C. M. *Phys. Rev. Lett.* **1984**, *52*, 2364–2367.
(18) Agranat, M. B.; Ashitkov, S. I.; Fortov, V. E.; Kirillin, A. V.; Kostanovskii, A. V.; Anisimov, S. I.; Kondratenko, P. S. *Appl. Phys. A* **1999**, *69*, 637–640.
(19) Lin, B.; Elsayed-Ali, H. E. *Surf. Sci.* **2002**, *498*, 275–284.
(20) Siwick, B. J.; Dwyer, J. R.; Jordan, R. E.; Miller, R. J. D. *Science* **2003**, *302*, 1382–1385.
(21) Sokolowski-Tinten, K.; Blome, C.; Blums, J.; Cavalleri, A.; Dietrich, C.; Tarasevich, A.; Uschmann, I.; Förster, E.; Kammler, M.; Horn-von-Hoegen, M.; von der Linde, D. *Nature (London)* **2003**, *422*, 287–289.
(22) Dwyer, J. R.; Hebeisen, C. T.; Ernstorfer, R.; Harb, M.; Deyirmenjian, V.; Jordan, R. E.; Miller, R. J. D. *Philos. Trans. R. Soc. London, Ser. A* **2006**, *364*, 741–778.
(23) Dwyer, J. R.; Jordan, R. E.; Hebeisen, C. T.; Harb, M.; Ernstorfer, R.; Dartigalongue, T.; Miller, R. J. D. *J. Mod. Opt.* **2007**, *54*, 905–922.
(24) Ruan, C. Y.; Murooka, Y.; Raman, R. K.; Murdick, R. A. *Nano Lett.* **2007**, *7*, 1290–1296.
(25) Chan, W. L.; Averback, R. S.; Cahill, D. G.; Lagoutchev, A. *Phys. Rev. B* **2008**, *78*, 214107.
(26) Ernstorfer, R.; Harb, M.; Hebeisen, C. T.; Sciaini, G.; Dartigalongue, T.; Miller, R. J. D. *Science* **2009**, *323*, 1033–1037.
(27) Richardson, C. F.; Clancy, P. *Mol. Simul.* **1991**, *7*, 335–355.
(28) Häkkinen, H.; Landman, U. *Phys. Rev. Lett.* **1993**, *71*, 1023–1026.
(29) Xu, X.; Cheng, C.; Chowdhury, I. H. *J. Heat Transfer* **2004**, *126*, 727–734.
(30) Zhigilei, L. V.; Ivanov, D. S. *Appl. Surf. Sci.* **2005**, *248*, 433–439.
(31) Lin, Z.; Johnson, R. A.; Zhigilei, L. V. *Phys. Rev. B* **2008**, *77*, 214108.
(32) Thomas, D. A.; Lin, Z.; Zhigilei, L. V.; Gurevich, E. L.; Kittel, S.; Hergenröder, R. *Appl. Surf. Sci.* **2009**, *255*, 9605–9612.
(33) Zhigilei, L. V.; Lin, Z.; Ivanov, D. S. *J. Phys. Chem. C* **2009**, *113*, 11892–11906.
(34) Ivanov, D. S.; Zhigilei, L. V. *Phys. Rev. B* **2003**, *68*, 064114.
(35) Ivanov, D. S.; Zhigilei, L. V. *Phys. Rev. Lett.* **2003**, *91*, 105701.
(36) Ivanov, D. S.; Zhigilei, L. V. *Appl. Phys. A* **2004**, *79*, 977–981.
(37) Upadhyay, A. K.; Urbassek, H. M. *J. Phys. D: Appl. Phys.* **2005**, *38*, 2933–2941.
(38) Lin, Z.; Zhigilei, L. V. *Phys. Rev. B* **2006**, *73*, 184113.
(39) Lin, Z.; Zhigilei, L. V. *J. Phys.: Conf. Ser.* **2007**, *59*, 11–15.
(40) Farkas, D.; Mohanty, S.; Monk, J. *Phys. Rev. Lett.* **2007**, *98*, 165502.
(41) Xiao, S.; Hu, W.; Yang, J. *J. Phys. Chem. B* **2005**, *109*, 20339–20342.
(42) Xiao, S.; Hu, W. *J. Chem. Phys.* **2006**, *125*, 014503.
(43) Lin, Z.; Zhigilei, L. V.; Celli, V. *Phys. Rev. B* **2008**, *77*, 075133.
(44) Lin Z.; Zhigilei, L. V. In *High-Power Laser Ablation VI*; Phipps, C. R., Ed.; *Proc. SPIE* **2006**, *6261*, 62610U.
(45) Okabe, A.; Boots, B.; Sugihara, K. *Spatial Tessellations: Concepts and Applications of Voronoi Diagrams*; John Wiley & Sons: Chichester, U.K., 1992.
(46) Schiøtz, J.; Vegge, T.; Di Tolla, F. D.; Jacobsen, K. W. *Phys. Rev. B* **1999**, *60*, 11971–11983.
(47) Van Swygenhoven, H.; Derlet, P. M.; Frøseth, A. G. *Nat. Mater.* **2004**, *3*, 399–403.
(48) Belonoshko, A. B.; Skorodumova, N. V.; Davis, S.; Osiptsov, A. N.; Rosengren, A.; Johansson, B. *Science* **2007**, *316*, 1603–1605.
(49) Kelchner, C.; Plimpton, S. J.; Hamilton, J. C. *Phys. Rev. B* **1998**, *58*, 11085–11088.
(50) Sakai, S.; Tanimoto, H.; Mizubayashi, H. *Acta Mater.* **1999**, *47*, 211–217.
(51) Kumar, S.; Kurtz, S. K.; Banavar, J. R.; Sharma, M. G. *J. Stat. Phys.* **1992**, *67*, 523–551.
(52) Egami, T.; Billinge, S. J. L. In *Underneath the Bragg Peaks. Structural analysis of complex material*; Cahn, R. W., Ed.; Pergamon Material Series; Elsevier: Oxford, U.K., 2003.
(53) Warren, B. E. *X-Ray Diffraction*; Addison-Wesley: Reading, MA, 1969.
(54) Anisimov, S. I.; Kapeliovich, B. L.; Perel'man, T. L. *Sov. Phys. JETP* **1974**, *39*, 375–377.
(55) Zhou, X. W.; Wadley, H. N. G.; Johnson, R. A.; Larson, D. J.; Tabat, N.; Cerezo, A.; Petford-Long, A. K.; Smith, G. D. W.; Clifton, P. H.; Martens, R. L.; Kelly, T. F. *Acta Mater.* **2001**, *49*, 4005–4015.
(56) *Smithell's Metal Reference Book*, 6th ed.; Brandes, E. A., Ed.; Butterworths: London, 1983.
(57) Morris, J. R.; Song, X. *J. Chem. Phys.* **2002**, *116*, 9352–9358.
(58) Qiu, T. Q.; Tien, C. L. *J. Heat Transfer* **1993**, *115*, 842–847.
(59) Hopkins, P. E. *J. Appl. Phys.* **2009**, *105*, 093517.
(60) Elsayed-Ali, H. E.; Juhasz, T.; Smith, G. O.; Bron, W. E. *Phys. Rev. B* **1991**, *43*, 4488–4491.
(61) Hostetler, J. L.; Smith, A. N.; Czajkowsky, D. M.; Norris, P. M. *Appl. Opt.* **1999**, *38*, 3614–3620.
(62) Huang, W. Y.; Qian, W.; El-Sayed, M. A.; Ding, Y.; Wang, Z. L. *J. Phys. Chem. C* **2007**, *111*, 10751–10757.
(63) Hohlfeld, J.; Wellershoff, S.-S.; Güdde, J.; Conrad, U.; Jähnke, V.; Matthias, E. *Chem. Phys.* **2000**, *251*, 237–258.
(64) Suárez, C.; Bron, W. E.; Juhasz, T. *Phys. Rev. Lett.* **1995**, *75*, 4536–4539.
(65) Liu, X.; Stock, R.; Rudolph, W. *Phys. Rev. B* **2005**, *72*, 195431.
(66) Zhigilei, L. V.; Garrison, B. J. *Appl. Phys. A* **1999**, *69*, S75–S80.
(67) Zhigilei, L. V.; Garrison, B. J. *J. Appl. Phys.* **2000**, *88*, 1281–1298.
(68) Anisimov, S. I.; Zhakhovskii, V. V.; Inogamov, N. A.; Nishihara, K.; Oparin, A. M.; Petrov, Yu. V. *JETP Lett.* **2003**, *77*, 606–610.
(69) Zhigilei, L. V.; Ivanov, D. S.; Leveugle, E.; Sadigh, B.; Bringa, E. M. In *High-Power Laser Ablation V*; Phipps, C. R., Ed.; *Proc. SPIE* **2004**, *5448*, 505−519.
(70) Leveugle, E.; Ivanov, D. S.; Zhigilei, L. V. *Appl. Phys. A* **2004**, *79*, 1643–1655.
(71) Garrison, B. J.; Itina, T. E.; Zhigilei, L. V. *Phys. Rev. E* **2003**, *68*, 041501.
(72) Park, H.; Wang, X.; Nie, S.; Clinite, R.; Cao, J. *Phys. Rev. B* **2005**, *72*, 100301.
(73) Shymanovich, U.; Nicoul, M.; Blums, J.; Sokolowski-Tinten, K.; Tarasevitch, A.; Wietler, T.; Horn von Hoegen, M.; von der Linde, D. *Appl. Phys. A* **2007**, *87*, 7–11.
(74) Harb, M.; Peng, W.; Sciaini, G.; Hebeisen, C. T.; Ernstorfer, R.; Eriksson, M. A.; Lagally, M. G.; Kruglik, S. G.; Miller, R. J. D. *Phys. Rev. B* **2009**, *79*, 094301.
(75) Luo, S.-N.; Ahrens, T. J.; Çağin, T.; Strachan, A.; Goddard III, W. A.; Swift, D. C. *Phys. Rev. B* **2003**, *68*, 134206.
(76) Belonoshko, A. B.; Skorodumova, N. V.; Rosengren, A.; Johansson, B. *Phys. Rev. B* **2006**, *73*, 012201.
(77) Porter, D. A.; Easterling, K. E. *Phase Transformations in Metals and Alloys*; Chapman & Hall: London, 1992.
(78) Forsblom, M.; Grimvall, G. *Nat. Mater.* **2005**, *4*, 388–390.
(79) Broughton, J. Q.; Gilmer, G. H. *J. Chem. Phys.* **1986**, *84*, 5759–5768.
(80) Davidchack, R. L.; Laird, B. B. *Phys. Rev. Lett.* **2000**, *85*, 4751–4754.
(81) Morris, J. R.; Song, X. *J. Chem. Phys.* **2003**, *119*, 3920–3925.
(82) Hoyt, J. J.; Asta, M.; Karma, A. *Phys. Rev. Lett.* **2001**, *86*, 5530–5533.
(83) Hoyt, J. J.; Asta, M. *Phys. Rev. B* **2002**, *65*, 214106.
(84) Hoyt, J. J.; Asta, M.; Karma, A. *Mater. Sci. Eng., R* **2003**, *41*, 121–163.
(85) Turnbull, D. *J. Appl. Phys.* **1950**, *21*, 1022–1028.
(86) Kelton K. F. In *Solid State Physics, Advances in Research and Applications*; Ehrenreich, H., Turnbull, D., Eds.; Academic Press: San Diego, CA, 1991; Vol. 45, pp 75−178.
(87) Bai, X. M.; Li, M. *J. Chem. Phys.* **2006**, *124*, 124707.
(88) Berendsen, H. J. C.; Postma, J. P. M.; van Gunsteren, W. F.; DiNola, A.; Haak, J. R. *J. Chem. Phys.* **1984**, *81*, 3684–3690.

JP909328Q